Quantifying Hydrodynamic Slip: A Comprehensive Analysis of Dewetting Profiles

R. Fetzer,*[,†,‡] A. Münch,[§,||] B. Wagner,[||] M. Rauscher,[⊥,#] and K. Jacobs[†]

Department of Experimental Physics, Saarland University, D-66123 Saarbrücken, Germany, Humboldt University of Berlin, Institute of Mathematics, Unter den Linden 6, D-10099 Berlin, Germany, Weierstrass Institute for Applied Analysis and Stochastics (WIAS), Mohrenstrasse 39, D-10117 Berlin, Germany, Max-Planck-Institute for Metals Research, Heisenbergstrasse 3, D-70569 Stuttgart, Germany, and Institute for Theoretical and Applied Physics, University of Stuttgart, Pfaffenwaldring 57, D-70569 Stuttgart, Germany

Received April 12, 2007. In Final Form: July 3, 2007

To characterize nontrivial boundary conditions of a liquid flowing past a solid, the slip length is commonly used as a measure. From the profile of a retracting liquid front (e.g., measured with atomic force microscopy), the slip length can be extracted with the help of a Stokes model for a thin liquid film dewetting from a solid substrate. Specifically, we use a lubrication model derived from the Stokes model for strong slippage and linearize the film profile around the flat, unperturbed film. For small slip lengths, we expand the linearized full Stokes model for small slopes up to third order. Using the respective model, we obtain, in addition to the slip length, the capillary number, from which we can estimate the viscosity of the fluid film. We compare numerical and experimental results, test the consistency and the validity of the models/approximations, and give an easy-to-follow guide of how they can be used to analyze experiments.

1. Introduction

In microfluidic devices, the drag of a fluid is a substantial concern because, for a given pumping power, it limits the microfluidic channel length that can be filled. It therefore also sets limits on, for example, the number of possible analysis steps to be performed in microfluidic immunoassays. Drag can be reduced by decreasing the friction at the liquid/solid interface, leading to an increase in the fluid velocity at the interface. This results in a sliding of the fluid over the solid and a nonzero boundary condition for the interface velocity. The amount of slippage is typically characterized by the depth b below the solid−liquid interface at which the extrapolated velocity vanishes.

To date, a number of methods exist to determine the slip length, with most of them involving tracer particles,[1,2] fluorescence recovery after photobleaching,[3,4] colloidal probe microscopy,[5,6] or surface forces apparatuses.[7,8] Detailed reviews can be found in recent articles by Lauga et al.[9] or Neto et al.[10] In our previous studies,[11−13] we introduced a new method of gaining interfacial flow properties, namely, the analysis of the profile of a liquid front. A discussion of viscoelastic effects can be found in the lubrication models that are derived and analyzed in refs 14−16 and 17 and 18, respectively. To induce the flow of a liquid film experimentally, we use the dewetting process.[19−21] The lubrication model that governs this process is derived in a systematic asymptotic expansion from the underlying Stokes equations together with appropriate boundary conditions at the free surface and at the liquid/solid interface. This enables us in turn to determine the validity of our new method based on the lubrication model for strong slippage and moreover to improve the method using a direct linearization of the Stokes model that is valid even for weak slippage. Specifically, we exploit the fact that the amount of slippage has a significant influence on the decay of the profile onto the unperturbed films, where the model equations can be linearized. A more comprehensive asymptotic analysis of the entire profile in the presence of large slippage, which necessarily must consider all nonlinearities, is a separate research direction (in part still ongoing).[22] For our purpose here, the information obtained from the linearized model(s) is sufficient to obtain the

* Corresponding author. E-mail: renate.fetzer@unisa.edu.au.
† Saarland University.
‡ Present address: Ian Wark Research Institute, University of South Australia, Mawson Lakes SA 5095, Australia.
§ Humboldt University of Berlin.
|| Weierstrass Institute for Applied Analysis and Stochastics (WIAS).
⊥ Max-Planck-Institute for Metals Research.
University of Stuttgart.

(1) Tretheway, D. C.; Meinhart, C. D. *Phys. Fluids* **2002**, *14*, L9. Tretheway, D. C.; Meinhart, C. D. *Phys. Fluids* **2004**, *16*, 1509.
(2) Lumma, D.; Best, A.; Gansen, A.; Feuillebois, F.; Radler, J. O.; Vinogradova, O. I. *Phys. Rev. E* **2003**, *67*, 056313.
(3) Pit, R.; Hervet, H.; Léger, L. *Phys. Rev. Lett.* **2000**, *85*, 980.
(4) Schmatko, T.; Hervet, H.; Léger, L. *Phys. Rev. Lett.* **2005**, *94*, 244501.
(5) Craig, V. S. J.; Neto, C.; Williams, D. R. M. *Phys. Rev. Lett.* **2001**, *87*, 054504.
(6) Vinogradova, O. I.; Yakubov, G. E. *Langmuir* **2003**, *19*, 1227.
(7) Cottin-Bizonne, C.; Jurine, S.; Baudry, J.; Crassous, J.; Restagno, F.; Charlaix, E. *Eur. Phys. J. E* **2002**, *9*, 47.
(8) Zhu, Y.; Granick, S. *Langmuir* **2002**, *18*, 10058.
(9) Lauga, E.; Brenner, M.; Stone, H. A. In *Handbook of Experimental Fluid Dynamics*; Foss, J., Tropea, C., Yarin, A., Eds.; Springer: New York, 2005.
(10) Neto, C.; Evans, D. R.; Bonaccurso, E.; Butt, H.-J.; Craig, V. S. J. *Rep. Prog. Phys.* **2005**, *68*, 2859.
(11) Fetzer, R.; Jacobs, K.; Münch, A.; Wagner, B.; Witelski, T. P. *Phys. Rev. Lett.* **2005**, *95*, 127801.
(12) Münch, A.; Wagner, B.; Witelski, T. P. *J. Eng. Math.* **2005**, *53*, 359.
(13) Fetzer, R.; Rauscher, M.; Münch, A.; Wagner, B. A.; Jacobs, K. *Europhys. Lett.* **2006**, *75*, 638.
(14) Rauscher, M.; Münch, A.; Blossey, R.; Wagner, B. *Eur. Phys. J. E* **2005**, *17*, 373.
(15) Blossey, R.; Münch, A.; Rauscher, M.; Wagner, B. *Eur. Phys. J. E* **2006**, *20*, 267.
(16) Münch, A.; Wagner, B.; Rauscher, M.; Blossey, R. *Eur. Phys. J. E* **2006**, *20*, 365.
(17) Vilmin, T.; Raphaël, E. *Eur. Phys. J. E* **2006**, *21*, 161.
(18) Hamieh, M.; Al Akhrass, S.; Hamieh, T.; Damman, P.; Gabriele, S.; Vilmin, T.; Raphaël, E.; Reiter, G. *J. Adhes.* **2007**, *83*, 367.
(19) Seemann, R.; Herminghaus, S.; Jacobs, K. *Phys. Rev. Lett.* **2001**, *86*, 5534.
(20) Redon, C.; Brochard-Wyart, F.; Rondelez, F. *Phys. Rev. Lett.* **1991**, *66*, 715.
(21) Reiter, G. *Phys. Rev. Lett.* **2001**, *87*, 186101.
(22) Evans, P. L.; King, J. R.; Münch, A. *AMRX Appl. Math. Res. Express* **2006**, *2006*, 25262.

10.1021/la7010698 CCC: $37.00
Published on Web 09/06/2007

slip length by fitting the eigenvalues that govern the decay of the profile to the experimentally measured film profiles. This method works well for viscous fluids dewetting from a solid surface.

To test the lubrication model, we also discuss here the full 2D description using the underlying Stokes model. We find that whereas the strong-slip lubrication model is valid in most of the interesting parameter regimes (i.e., where changes in slippage have a significant impact on the film profile), the validity can be extended to smaller slip lengths by using a third-order Taylor expansion for small slopes for the eigenvalue relation characterizing the linearized film profile. The third-order Taylor expansion of the Stokes model is able to extract the slip length and capillary number quite accurately from experiments on dewetting fluids where the form of the profile is accessible, for example, by atomic force microscopy (AFM). Via the capillary number, the viscosity can be obtained if the dewetting velocity and the surface tension are known. In the following text, we will develop the theoretical approach, compare numerical and experimental results, introduce the Stokes model and its approximations, test their validity, and give a description of how they can be used to analyze experiments.

2. Formulation

Recently we have shown that the dewetting process of highly viscous polystyrene (PS) melts on hydrophobized silicon wafers is well described by a lubrication model in the regime of large slip lengths.[11,13] For the situation considered here, the flow is very slow, and inertia terms will not play any role. For the analyzed stage of dewetting, the shear rate is also low, which results in Weissenberg numbers below 0.07 for the short-chain PS films investigated. Therefore, non-Newtonian properties such as the viscoelasticity of the melt can be neglected.[23] For clarity of presentation and as in our previous studies, we will consider the effectively 2D situation of a liquid ridge, which is translationally invariant in the Y direction parallel to the flat, homogeneous substrate. Hence, we begin our theoretical discussion with the Stokes equations for an incompressible fluid layer on $0 \le Z \le H(X, T)$ in two dimensions

$$-\nabla P + \eta\nabla^2\mathbf{U} = 0 \qquad \nabla\cdot\mathbf{U} = 0 \tag{1}$$

together with appropriate boundary conditions (see below). Here, $\mathbf{U} = U(X, Z, T)\hat{\boldsymbol{e}}_x + W(X, Z, T)\hat{\boldsymbol{e}}_z$ denotes the velocity field, η denotes the viscosity, and $P = P(X, Z, T)$ is the pressure field.

At the free surface $Z = H(X, T)$, we have the usual kinematic condition for nonvolative fluids

$$\partial_T H = -\partial_X \int_0^H U(X, Z)\, \mathrm{d}Z \tag{2}$$

and normal and tangential stress boundary conditions with constant surface tension σ

$$\boldsymbol{n}\cdot\tau\cdot\boldsymbol{n} - (P - \Phi'(H)) = 2\sigma\kappa \quad \text{and} \quad \boldsymbol{n}\cdot\tau\cdot\boldsymbol{t} = 0 \tag{3}$$

with the stress tensor

$$\tau = \eta[\nabla\mathbf{U} + (\nabla\mathbf{U})^T] \tag{4}$$

and where $\Phi'(H) = \mathrm{d}\Phi/\mathrm{d}H$ denotes the contribution due to the effective interface potential $\Phi(H)$ (of the Born/van der Waals type). See ref 19 for details of the potential. The normal and tangential unit vectors are given by

$$\boldsymbol{n} = \frac{(-\partial_X H, 1)}{\sqrt{1 + (\partial_X H)^2}} \quad \text{and} \quad \boldsymbol{t} = \frac{(1, \partial_X H)}{\sqrt{1 + (\partial_X H)^2}} \tag{5}$$

where the local mean curvature is $\kappa = \nabla\cdot\boldsymbol{n}$. At $Z = 0$, we assume the impermeability of the substrate and the Navier slip boundary condition

$$W = 0 \quad \text{and} \quad U = B\,\partial_Z U \tag{6}$$

respectively, with Navier slip length B.

We nondimensionalize the above system of equations using the following scales:

$$\begin{aligned} &Z = \bar{H}z, \quad X = \bar{L}x, \quad H = \bar{H}h, \quad B = \bar{H}b, \\ &U = \bar{U}u, \quad W = \bar{W}w, \quad T = (\bar{H}/\bar{W})t, \quad P = \bar{P}p, \\ &\Phi' = \bar{P}\phi' \end{aligned} \tag{7}$$

The vertical length scale $\bar{H}$ is fixed by the average film thickness, and the lateral length scale $\bar{L}$ is fixed by the competition of the effective interface potential and the surface tension (i.e., by the dispersive capillary length). The vertical and horizontal velocity scales are linked via the incompressibility condition $\bar{U} = \bar{L}\,\bar{W}/\bar{H}$. The choice of the pressure scale $\bar{P}$ and the velocity scale $\bar{U}$ together with the magnitude of b fixes the flow regime.

In ref 12, it is shown that for large slip lengths (i.e., for $b \gg 1$) the scale separation $\bar{H}/\bar{L} = \epsilon \ll 1$ allows for the derivation of a simplified lubrication model, where the flow field is essentially plug flow. This implies a balance of the pressure gradient with the dominant viscosity contribution in the vertical momentum equation, which yields the scaling

$$\frac{\bar{P}\bar{H}}{\eta\bar{U}} \sim \epsilon$$

We assume that surface tension and pressure balance the normal shear stress (and therefore surface tension does play a role in the dynamics of the film)

$$\frac{\sigma}{\bar{P}\,\bar{H}} \sim \epsilon^{-2}$$

so that

$$\bar{U} = \frac{\sigma\epsilon}{\eta} \quad \text{and} \quad \mathrm{Ca} = \frac{\eta\bar{U}}{\sigma} = \epsilon \tag{8}$$

In addition, we assume that $b = \beta/\epsilon^2$ with $\beta = O(\epsilon^0)$ (i.e., that the slip length is large compared to the lateral length scale $\bar{L}$). The nondimensional problem in strong-slip scaling is therefore

$$-\epsilon^2\partial_x p + \epsilon^2\partial_x{}^2 u + \partial_z{}^2 u = 0 \tag{9}$$

$$-\partial_z p + \epsilon^2\partial_x{}^2 w + \partial_z{}^2 w = 0 \tag{10}$$

$$\partial_x u + \partial_z w = 0 \tag{11}$$

with boundary conditions at $z = h(x, t)$

$$\partial_t h - w + u\partial_x h = 0 \tag{12}$$

$$(\partial_z u + \epsilon^2\partial_x w)(1 - \epsilon^2(\partial_x h)^2) + 2\epsilon^2\partial_x h(\partial_z w - \partial_x u) = 0 \tag{13}$$

(23) Note that in the very early stage of dewetting viscoelastic effects may become visible.

$$p - \phi'(h) - 2\frac{(1-\epsilon^2(\partial_x h)^2)\partial_z w - \partial_x h(\partial_z u + \epsilon^2 \partial_x w)}{1+\epsilon^2(\partial_x h)^2} + \frac{\partial_x{}^2 h}{(1+\epsilon^2(\partial_x h)^2)^{3/2}} = 0 \quad (14)$$

and boundary conditions at $z = 0$

$$w = 0 \text{ and } u = b\partial_z u = \frac{\beta}{\epsilon^2}\partial_z u \quad (15)$$

As shown in detail in ref 12, assuming that u, w, p and h have the asymptotic expansions

$$u(x, z, t; \epsilon) = u_0(x, z, t) + \epsilon^2 u_1(x, z, t) + O(\epsilon^4) \quad (16)$$

$$w(x, z, t; \epsilon) = w_0(x, z, t) + \epsilon^2 w_1(x, z, t) + O(\epsilon^4) \quad (17)$$

$$p(x, z, t; \epsilon) = p_0(x, z, t) + \epsilon^2 p_1(x, z, t) + O(\epsilon^4) \quad (18)$$

$$h(x, t; \epsilon) = h_0(x, t) + \epsilon^2 h_1(x, t) + O(\epsilon^4) \quad (19)$$

and integrating the problem to $O(\epsilon^2)$, the lubrication model for strong slip is found to be

$$\frac{4}{h_0}\partial_x(h_0\,\partial_x u_0) + \partial_x(\partial_x{}^2 h_0 - \phi'(h_0)) - \frac{u_0}{\beta\, h_0} = 0 \quad (20)$$

where the solution of the leading-order problem implies that $u_0 = u_0(x, t)$. The first term on the left side is proportional to the divergence of the total longitudinal shear stress integrated over the film thickness. The second term is the gradient of pressure in the film. This equation, coupled with the kinematic condition (eq 2)

$$\partial_t h_0 + \partial_x(h_0\, u_0) = 0 \quad (21)$$

gives a closed system for $u_0(x, t)$ and $h_0(x, t)$, which is called the strong-slip model.[12]

3. Experiments and Comparison with Numerical Results

To test the theoretical strong-slip model, we performed dewetting experiments with thin films of short-chained polystyrene (PS) on top of hydrophobized silicon wafers. We achieved 130-nm-thick films of atactic PS (molecular weight 13.7 kg/mol, $M_w/M_n = 1.03$, PSS Mainz, Germany) by spin coating a toluene solution on mica, floating the films on fresh Millipore water, and transferring them onto the coated wafers. To hydrophobize the substrates, we coated silicon wafers (2.1 nm native oxide layer, Wacker, Burghausen, Germany) with two different silane monolayers, octadecyltrichlorosilane (OTS) and the shorter dodecyltrichlorosilane (DTS), using standard techniques.[24] The rms roughness of both types of substrates as measured by atomic force microscopy (AFM) at 1 μm^2 scan size is below 0.15 nm. The contact angle of polystyrene droplets is 67-(3)° on both coatings, as AFM scans revealed.

To mobilize the films that are glassy at room temperature, we heated the samples to different temperatures (105−130 °C) above the glass-transition temperature of PS(13.7k), $T_g = 97$ °C. The dewetting process sets in by the nucleation of holes, which instantaneously start to grow. The actual nucleation mechanism (homogeneous or heterogeneous) is irrelevant here, because we will analyze only the shape of the dewetting rim around the hole. We observed the growth of holes by optical microscopy to determine the dewetting velocity. Once the holes had a radius of 12 μm, we rapidly quenched the samples to room temperature and measured the profiles of the holes with an atomic force microscope (AFM). See Figure 1 for a typical image.

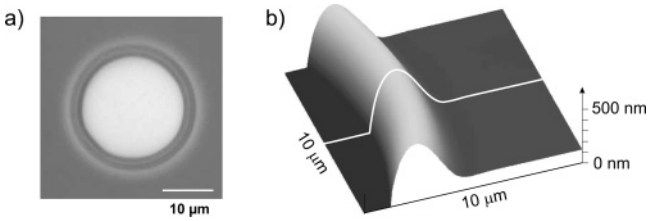

Figure 1. (a) Optical image of a hole in a 130-nm-thick PS(13.7k) film, dewetted from OTS on Si at 120 °C. (b) AFM image of a section of the rim around the hole shown in part a. A cross section taken in radial direction (indicated by the white line) gives the rim profile that will be compared to theory.

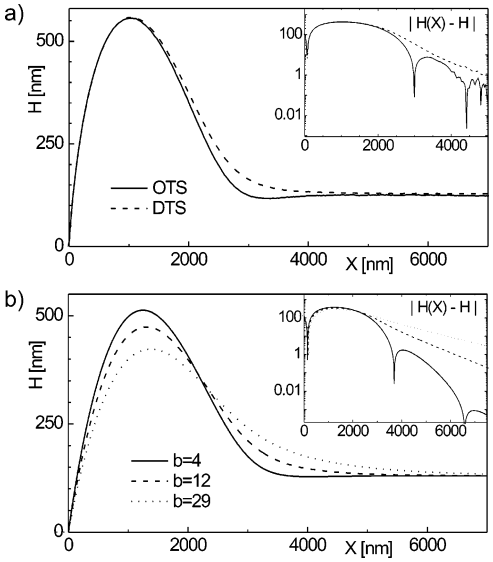

Figure 2. (a) Rim profiles of holes of radius 12 μm in 130-nm-thick PS(13.7k) films dewetted at 120 °C. Depending on the substrate, OTS- or DTS-covered Si wafers, the profiles show an oscillatory or monotonic decay toward the undisturbed film. (b) Rim profiles calculated from the lubrication model for different slip lengths b nondimensionalized with $\bar{H} = 130$ nm.

By comparing the profiles for PS films on OTS- and DTS-covered wafers at identical temperature, we find substantial differences, as shown in Figure 2a for 120 °C. Films on DTS exhibit a rim profile that decays monotonically toward the undisturbed film, whereas a film on the OTS layer exhibits an oscillatory decaying rim shape. To clarify the different rim morphologies, the inset to Figure 2a depicts $|H(X) - \bar{H}|$ in a semilogarithmic plot. Here, $\bar{H}$ denotes the prepared film-thickness.

In Figure 2b, rim profiles calculated by the lubrication model (eqs 20 and 21) are shown for different slip lengths. For details of the simulations, we refer to refs 12 and 25. By increasing the slip length b, we can observe a transition from oscillatory to monotonically decaying rim profiles.

To understand this morphological transition of rim shapes observed in both the experiments and the simulations, we concentrate in the next section on the region where the rim connects to the undisturbed film and develop theoretical models to describe rim profiles.

4. Linear Stability Analysis of the Undisturbed Uniform Film

The structure of the dewetting rim as it propagates into the undisturbed film can be found via linearized analysis. Note that

(24) Wassermann, S. R.; Tao, Y.-T.; Whitesides, G. M. *Langmuir* **1989**, *5*, 1074.

(25) Münch, A. *J. Phys.: Condens. Matter* **2005**, *17*, S309.

for later comparison with experiments the contribution from the intermolecular potential can be neglected. In the following text, we analyze the shape of the rim close to the resting film. There, the film thickness is still close to the thickness of the flat resting film, which will be the base state. We linearize about this base state with respect to infinitesimal perturbations of the film thickness, flow velocity, and so forth of size δ and obtain the shape of the leading edge of the rim.

4.1. Lubrication Model. The base state of the strong-slip model in eqs 20 and 21 is $h(x, t) = 1$, $u(x, t) = 0$, about which we linearize with respect to infinitesimal perturbations of size δ

$$h(x, t) \approx 1 + \delta\tilde{h}(x, t), \quad u(x, t) \approx \delta\tilde{u}(x, t), \quad \delta \ll 1 \tag{22}$$

to obtain the linearized equations

$$4\partial_x{}^2\tilde{u} + \partial_x{}^3\tilde{h} - \frac{1}{\beta}\tilde{u} = 0 \tag{23}$$

$$\partial_t\tilde{h} + \partial_x\tilde{u} = 0 \tag{24}$$

To describe the advancing edge of the ridge, it is convenient to shift to a frame of reference that is moving in concert with the ridge, $\xi = x - s(t)$, and seek quasi-stationary solutions in the form of travelling fronts, $\tilde{h} = \tilde{h}(\xi)$. Then, the continuity equation (eq 24) forces $\tilde{u} = \dot{s}\tilde{h}(\xi)$. Inserting this into the momentum equation (eq 23) yields

$$4\dot{s}\,\partial_\xi{}^2\tilde{h} + \partial_\xi{}^3\tilde{h} - \frac{\dot{s}}{\beta}\tilde{h} = 0 \tag{25}$$

To understand the qualitative forms of the advancing ridge in this equation, we solve it with the ansatz $\tilde{h}(\xi) = \hat{h}\exp(\gamma\xi)$, yielding the characteristic equation

$$\chi_{\mathrm{lub}}(\gamma; \beta, \dot{s}) = \gamma^3 + 4\,\dot{s}\gamma^2 - \frac{\dot{s}}{\beta} = 0 \tag{26}$$

Note that in this equation γ depends on t parametrically through $s(t)$.

For the transitions in the ridge structure, we note that Descartes' law of signs shows that there is one positive real root and either two negative or two complex conjugate roots. Physically relevant solutions, with $\tilde{h}(\xi \to \infty) \to 0$, must have $\mathscr{R}(\gamma) < 0$. The change in roots from real to complex conjugate occurs when the discriminant vanishes, equivalently,

$$1 - \frac{256}{27}\beta\,\dot{s}^2 = 0 \tag{27}$$

From eq 27, we obtain an estimate of the critical ridge speed that separates real decaying profiles (γ real) from oscillatory profiles (complex conjugate γ) in terms of the slippage

$$\dot{s}_{\mathrm{crit}} \approx \sqrt{\frac{3}{\beta}}\frac{3}{16} \tag{28}$$

4.2. Stokes Model. To show the range of validity and applicability of this result, it is instructive to go back to the full Stokes model. We start with eqs 9−15 (i.e., the Stokes model in the strong-slip scaling), but we keep all terms.

In two dimensions, it is convenient to express the flow velocities in terms of the stream function

$$\partial_z\psi = u \quad \text{and} \quad -\partial_x\psi = w \tag{29}$$

Then we can formulate the incompressible Stokes problem in eqs 9−11 coupled to the kinematic condition in eq 12 in terms of ψ and h. For the incompressible Stokes equations (eqs 9−11), we get

$$\partial_z{}^4\psi + 2\epsilon^2\partial_x{}^2\partial_z{}^2\psi + \epsilon^4\partial_x{}^4\psi = 0 \tag{30}$$

The boundary conditions at the film surface $z = h$ in eqs 12−14 become

$$\partial_t h + \frac{\mathrm{d}}{\mathrm{d}x}\psi(x, h, t) = 0 \tag{31}$$

$$(\partial_z{}^2\psi - \epsilon^2\partial_x{}^2\psi)(1 - \epsilon^2(\partial_x h)^2) - 4\epsilon^2\partial_x h\partial_x\partial_z\psi = 0 \tag{32}$$

$$\epsilon^2\partial_x{}^2\partial_z\psi + \partial_z{}^3\psi - (\epsilon^4\partial_x{}^3\psi + \epsilon^2\partial_x\partial_z{}^2\psi)\partial_x h + \epsilon^2\frac{\mathrm{d}}{\mathrm{d}x}\frac{\partial_x{}^2 h}{(1 + \epsilon^2(\partial_x h)^2)^{3/2}} - 2\epsilon^2\frac{\partial}{\partial x}\frac{-(1 - \epsilon^2(\partial_x h)^2)\partial_x\partial_z\psi - \partial_x h(\partial_z{}^2\psi - \epsilon^2\partial_x{}^2\psi)}{1 + \epsilon^2(\partial_x h)^2} = 0 \tag{33}$$

respectively. Note that in order to be able to express the pressure in terms of ψ via eqs 9 and 10, eq 33 is the total derivative of eq 14 with respect to x. At $z = 0$, we get from eq 15

$$\psi = 0 \quad \text{and} \quad \partial_z\psi - b\partial_z{}^2\psi = 0 \tag{34}$$

As in the previous section, we now linearize about the undisturbed base state $h = 1$, $\psi = 0$ (i.e., about the flat, resting film) by perturbing via

$$h = 1 + \delta\tilde{h} \quad \text{and} \quad \psi = \delta\tilde{\psi} \tag{35}$$

with $\delta \ll 1$. We then transform to the moving-frame coordinate $\xi = x - s(t)$ and use the ansatz

$$\tilde{\psi}(x, z, t) = \hat{\psi}(z)\exp(\gamma\xi) \quad \text{and} \quad \tilde{h}(x, t) = \hat{h}\exp(\gamma\xi) \tag{36}$$

Keeping only the $O(\delta)$ terms, we obtain the linearized problem for the full Stokes model in eq 30

$$\partial_z{}^4\hat{\psi} + 2(\epsilon\gamma)^2\partial_z{}^2\hat{\psi} + (\epsilon\gamma)^4\hat{\psi} = 0 \tag{37}$$

in $0 < z < 1$, with boundary conditions at the film surface at $z = 1$ (corresponding to eqs 32 and 33)

$$(\epsilon\gamma)^2\hat{\psi} - \partial_z{}^2\hat{\psi} = 0 \tag{38}$$

$$3(\epsilon\gamma)^2\partial_z\hat{\psi} + \frac{(\epsilon\gamma)^3}{\epsilon\,\dot{s}}\hat{\psi} + \partial_z{}^3\hat{\psi} = 0 \tag{39}$$

and at the substrate surface at $z = 0$ (derived from eq 34)

$$\hat{\psi} = 0 \quad \text{and} \quad \partial_z\hat{\psi} - b\partial_z{}^2\hat{\psi} = 0 \tag{40}$$

The general solution for the linear ordinary differential equation in eq 37 is

$$\hat{\psi}(z) = c_1\mathrm{e}^{\mathrm{i}\epsilon\gamma z} + c_2\mathrm{e}^{-\mathrm{i}\epsilon\gamma z} + c_3 z\mathrm{e}^{\mathrm{i}\epsilon\gamma z} + c_4 z\mathrm{e}^{-\mathrm{i}\epsilon\gamma z} \tag{41}$$

Inserting this into the boundary conditions (eqs 38−40) yields a system of linear homogeneous equations for coefficients c_1, ..., c_4. This system has a nontrivial solution, indicating an eigensolution of eqs 37−40 if the determinant of this system is zero. The determinant is easily found to be (after multiplication with $\dot{s}b(\epsilon\gamma)^4/16$)

$$\chi_S(\gamma; b, \dot{s}) = \left(-\epsilon^2\dot{s}\gamma + \frac{1}{4b}\right)\sin(2\epsilon\gamma) + \left(\frac{\epsilon\dot{s}}{2b} + \frac{\epsilon\gamma}{2}\right)\cos(2\epsilon\gamma) - 2\left(1 + \frac{1}{2b}\right)\epsilon\dot{s}(\epsilon\gamma)^2 - \left(\frac{1}{2} + \frac{1}{2b}\right)\epsilon\gamma + \frac{\epsilon\dot{s}}{2b} \quad (42)$$

For eq 42, we seek the solutions γ that have a negative real part because we require that the perturbed profile be $\tilde{h}(x, t) \to 1$ as $x \to \infty$. Furthermore, we focus on the case where the decay is consistent with the basic assumption of lubrication theory, namely, that the length scale ratio, measured, for example, by the typical spatial derivative of the unscaled film thickness, is of order ϵ. For the scale variable $\tilde{h}(x, t)$ given in eq 36, this can be satisfied by requiring that $\tilde{h}_x/h = \gamma$ is of order 1.

Thus, $\epsilon\gamma$ is assumed to be small, and we can approximate χ_S by its Taylor expansion for $\epsilon\gamma \ll 1$.

$$\chi_T(\gamma; b, \dot{s}) = \left(1 + \frac{1}{3b}\right)(\epsilon\gamma)^3 + 4\epsilon\dot{s}\left(1 + \frac{1}{2b}\right)(\epsilon\gamma)^2 - \frac{\epsilon\dot{s}}{b} = 0 \quad (43)$$

If we now recall $b = \beta/\epsilon^2$ for the strong-slip regime and take the limit $\epsilon \to 0$ keeping $\beta = O(1)$ fixed, we obtain to leading order the characteristic equation $\chi_{lub}(\gamma; \beta, \dot{s})$ for the strong-slip lubrication model (i.e., eq 26).

Before proceeding, let us note that by rescaling the dewetting speed to $\dot{s} = \epsilon^2\dot{s}^*$, taking the limit $\epsilon \to 0$, and keeping $\dot{s}^* = O(1)$ and $b = O(1)$ fixed (in contrast to scaling $b = \beta/\epsilon^2$ with $\beta = O(1)$ in the rest of the article), one finds to leading order in ϵ the characteristic equation for the weak-slip regime

$$\chi_{weak}(\gamma; b, \dot{s}^*) = \gamma^3 - \frac{\dot{s}^*}{b + 1/3} = 0 \quad (44)$$

Next, we focus on the two dominant decaying modes γ_1 and γ_2 for the spatial decay of the film profile for each of the three characteristic equations (i.e., χ_{lub}, χ_S, and χ_T). These modes are given by $\chi = 0$ with $Re(\gamma) < 0$ for which the modulus is the smallest. They can be either two real negative or a complex conjugate pair of values. Note that χ_T and χ_{lub} are cubic polynomials with at most three zeros and χ_S is a transcendental equation that can have infinitely many solutions for $\chi_S = 0$.

An inspection of these two dominant modes shows that for each of the three χ's the eigenvalues are complex conjugates for $(b, \dot{s})$ below a certain line and real above it. The line is characterized by a merging of the two values to one real double root of the equation, in other words, for those $(b, \dot{s}(b))$ that satisfy

$$\chi(\gamma; b, \dot{s}) = 0 \quad \text{and} \quad \frac{d}{d\gamma}\chi(\gamma; b, \dot{s}) = 0 \quad (45)$$

For χ_S, these equations have to be solved numerically to obtain $\epsilon\dot{s}^S_{crit}(b)$ whereas for χ_T and χ_{lub} we obtain

$$\epsilon\dot{s}^T_{crit} = \frac{3\sqrt{3}}{16}\frac{b + 1/3}{(b + 1/2)^{3/2}} \quad (46)$$

$$\epsilon\dot{s}^{lub}_{crit} = \frac{3\sqrt{3}}{16}b^{-1/2} \quad (47)$$

respectively. The comparison is made in Figure 3 and shows that the result for $\epsilon\dot{s}^T_{crit}$ yields a good approximation for the curve $\epsilon\dot{s}^S_{crit}(b)$ of the full model for all values of b whereas the approximation quality of $\epsilon\dot{s}^{lub}_{crit}$ obtained from the strong-slip lubrication model deteriorates for small b as expected.

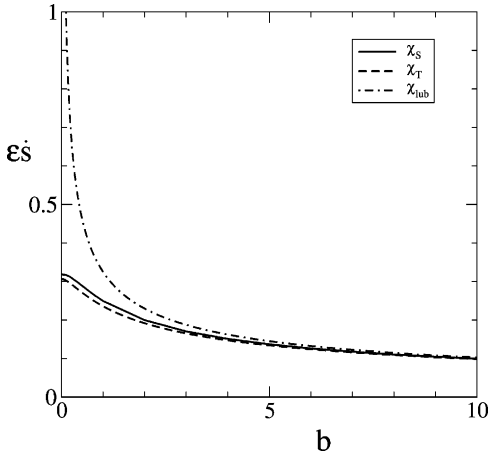

Figure 3. Comparison of the critical $\dot{s}(b)$, given by eq 45, at which the dominant eigenvalues γ that govern the spatial decay of the film profile change from complex conjugates (for $\dot{s} < \dot{s}_{crit}(b)$) to two real eigenvalues (for $\dot{s} > \dot{s}_{crit}(b)$). The solid, dashed, and dashed-dotted lines are, respectively, the critical $\dot{s}_{crit}(b)$ for the eigenvalues obtained for the full Stokes model (i.e., $\chi = \chi_S$), for third-order Taylor approximation of χ_S (i.e, $\chi = \chi_T$) and for the strong-slip lubrication model, where $\chi = \chi_{lub}$.

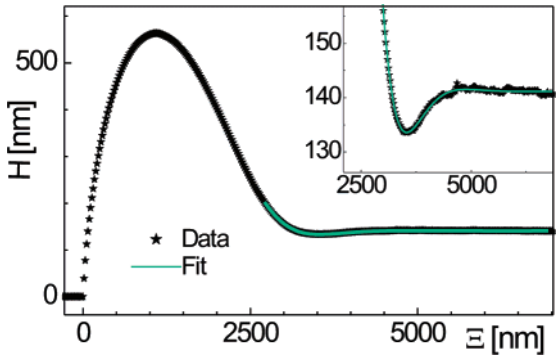

Figure 4. Profile of the rim shown in Figure 1 in the region where it decays toward the undisturbed film (i.e., for small perturbations) is well fit by an exponentially decaying oscillation.

5. Method to Quantify Slippage and Its Validity

5.1. Method. The process of determining the slip length from the shape of a moving rim essentially reverses the above considerations: from the experimentally measured rim shape, the two dominant decaying spatial modes γ_1 and γ_2 are extracted. Using these values, the slip length B and the capillary number Ca can be determined from the characteristic equation $\chi = 0$. As the full Stokes model χ_S ends up in quite cumbersome expressions for B and Ca, we focus in the following section on the strong-slip lubrication model.

To get the values for γ_1 and γ_2 (or rather their dimensional form $\Gamma_{1,2} = \gamma_{1,2}/\bar{L}$) from the experimentally observed rim profiles, one has to fit the respective function $H(\Xi) = \bar{H} + \delta\tilde{H}(\Xi)$ to the data in the region of small perturbations of the undisturbed film of thickness $\bar{H}$. Note that $\Xi = \bar{L}\xi$ denotes the dimensional form of the abscissa ξ. For the least-squares fitting procedure, we used data points of the profiles up to a maximal height of about 120% of $\bar{H}$. In the case of oscillatory decaying profiles, Γ_1 and Γ_2 are a pair of complex conjugate numbers $\Gamma_{1,2} = \Gamma_r \pm i\Gamma_i$ with negative Γ_r. Here, an exponentially damped oscillation $\delta\tilde{H}_{osc} = \delta\tilde{H}_0 \exp(\Gamma_r\Xi)\cos(\Gamma_i\Xi + \phi)$ (fit parameters are $\delta\tilde{H}_0$, Γ_i, Γ_r, and ϕ) captures the decay toward the resting film thickness $\bar{H}$ in the experimental data very well (Figure 4). From the fit, we gain the inverse decay length Γ_r and the wave number Γ_i, and thus $\Gamma_{1,2} = \Gamma_r \pm i\Gamma_i$. In the case of monotonically decaying rims, the data

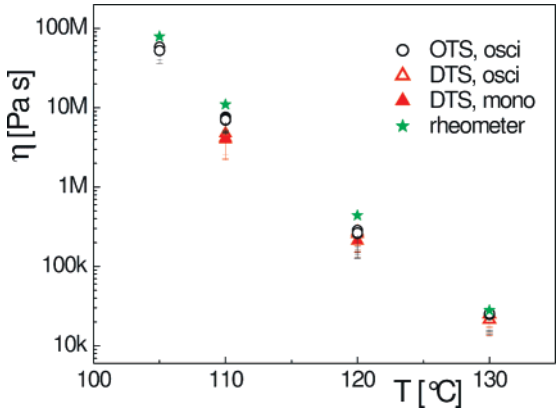

Figure 5. Viscosity as a function of temperature. The results of rim shape analysis of PS films on OTS and DTS are compared with viscosity data from independent rheometric measurements; "osci" and "mono" indicate fitting functions $\delta\tilde{H}_{osc}$ and $\delta\tilde{H}_{mon}$ that are used, respectively.

can be fitted by a superposition of two exponentials $\delta\tilde{H}_{mon} = \delta\tilde{H}_1\exp(\Gamma_1\Xi) + \delta\tilde{H}_2\exp(\Gamma_2\Xi)$ (fit parameters $\delta\tilde{H}_{1,2}$ and $\Gamma_{1,2}$) with inverse decay lengths Γ_1 and Γ_2.

After extracting Γ_1 and Γ_2, these values can now be used to determine the slip length and the capillary number of the investigated system. For this purpose, we recall the characteristic equation of the strong-slip lubrication model (eq 26) in dimensional form

$$\chi_{lub}(\Gamma; B, Ca) = (\bar{H}\Gamma)^3 + 4Ca(\bar{H}\Gamma)^2 - Ca\frac{\bar{H}}{B} = 0 \quad (48)$$

where the capillary number is $Ca = \eta\dot{S}/\sigma$ with the characteristic speed of the rim $\dot{S} = \bar{U}\dot{s}$. By knowing two roots Γ_1 and Γ_2 of eq 48, we get two equations with two unknowns B and Ca for which we can solve and get

$$B_{lub} = \frac{1}{4\bar{H}}\frac{\Gamma_1^2 + \Gamma_1\Gamma_2 + \Gamma_2^2}{\Gamma_1^2\Gamma_2^2},$$

$$Ca_{lub} = -\frac{\bar{H}}{4}\frac{\Gamma_1^2 + \Gamma_1\Gamma_2 + \Gamma_2^2}{\Gamma_1 + \Gamma_2} \quad (49)$$

Additionally, the film viscosity η can be determined from Ca using the surface tension $\sigma = 30.8$ mN/m and the observed dewetting velocity $\dot{S}$. We emphasize that to determine only the slip length, knowledge of neither the dewetting velocity nor the viscosity is required.

To check the consistency of the above-explained analysis, we performed a couple of tests with the experimental data. First, we determined the viscosity from the extracted capillary number from profiles on OTS and DTS at different temperatures. The viscosity was found to be in line with rheometric data (Figure 5). A second test was the variation of film thickness, which leads to different values for $\Gamma_{1,2}$ and $\dot{S}$ but does not change the slip length and the viscosity. Indeed, the extracted slip length was independent of the initial film thickness. In a third and last consistency check, we analyzed holes of various sizes. With growing hole diameter, the rim gets larger. As friction forces increase with rim size, the dewetting velocity slows down. As a consequence, a more pronounced oscillatory shape can be found, resulting in a variation of Γ_1 and Γ_2 with hole size. However, the slip lengths and viscosities obtained via eq 49 were independent of the hole size as expected. For details, refer to ref 13.

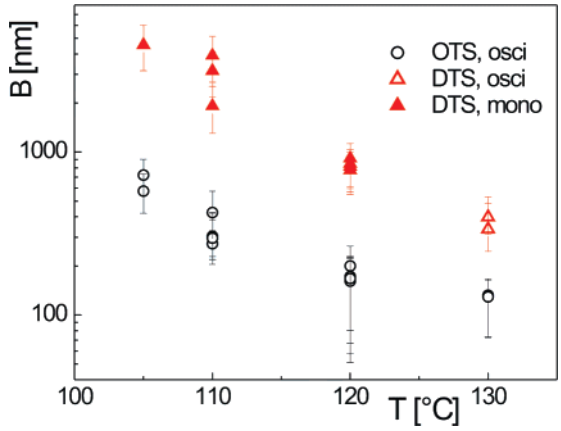

Figure 6. Slip length B for PS(13.7k) on OTS and DTS coatings as a function of melt temperature. The data are extracted from rim profiles of holes of radius 12 μm in 130-nm-thick films.

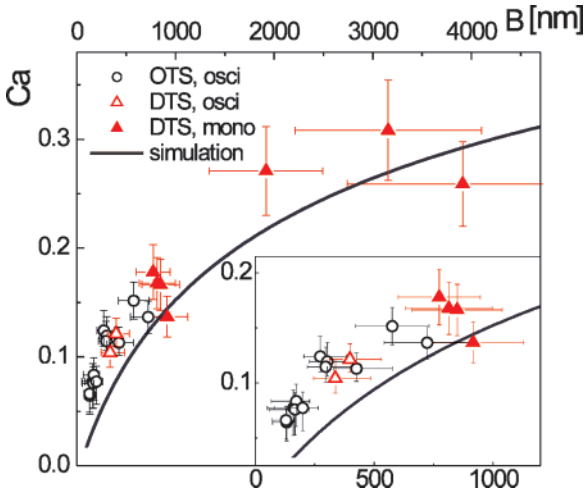

Figure 7. Capillary number Ca extracted from the rims analyzed in Figure 6. In the plot of Ca versus the respective slip lengths, the data collapses onto one curve. The solid line indicates the result of simulations. The inset depicts an enlargement of the region of slip lengths below 1 μm.

5.2. Results and Discussion. All tests performed in the previous section show consistent results for both the viscosity and the slip length. Therefore, we can rely on the analysis method. In Figure 6, the results for polystyrene films of constant molecular weight (13.7 kg/mol) and constant initial film thickness (130 nm) are summarized. All data shown here are extracted from rims of the same volume. As indicated by the error bars, there is no systematic difference in the accuracy of the gained results between oscillatory and monotonically decaying profiles up to slip lengths of about 1 μm. However, the results are less accurate for still larger slip lengths. (See also section 5.3). We find that the amount of slippage depends on both the substrate underneath and the melt temperature. For polystyrene films on the DTS coating, the slip length is about 1 order of magnitude larger than on OTS. On both coatings, however, slippage decreases for increasing melt temperature.

Plotting the capillary number obtained by rim shape analysis versus the slip length, as shown in Figure 7, we find that the data from different substrates collapses on one curve. By varying the dewetting temperature or the type of substrate underneath, we can change the amount of slippage and hence probe this curve successively. As expected, the dewetting velocity $\dot{S}$ and with it the capillary number $Ca = \eta\dot{S}/\sigma$ increase for increasing slip length, but this behavior is found to be clearly nonlinear.

From the simulations shown in Figure 2b, which were based on the lubrication model in eqs 20 and 21, we can in addition to the rim profile calculate the dewetting velocity $\dot{S}$ at the stage when the rim size matches that of the experiments. Doing this for different slip lengths, we gain the capillary number as function of B. This curve is shown in Figure 7 as the solid line. The qualitative behavior is in good agreement with the experimental data. However, a shift to lower capillary numbers can be observed. This may have various causes. First, the calculation was made for straight fronts whereas in the experiments the growth of circular holes is investigated. For the analyzed experiments with hole radii of 12 μm, however, the curvature of the contact line is negligible compared to the curvature of the rim in the radial direction. Second, in the simulations only the linearized curvature of the long-wave approximation was taken into account.

Results for the weak slip model with linearized curvature and with nonlinear curvature in the expression for the surface tension suggest that the former tends to underestimate the dewetting rate.[25,26] This is consistent with the observation that higher contact angles are typically associated with higher dewetting rates[20,25,27] and the inclusion of nonlinear curvature generally leads to higher contact angles. The static contact angle θ_S for the nonlinear curvature case is given by

$$1 - (1 + \tan^2 \theta_S)^{-1/2} = -\frac{1}{\sigma}\min_h \phi(h)$$

or

$$1 - \cos \theta_S = -\frac{1}{\sigma}\min_h \phi(h) \tag{50}$$

(see, for example, ref 19), and from this we obtain for the linearized curvature case ($\tan \theta_S \ll 1$)

$$\frac{1}{2}\tan^2 \theta_S = -\frac{1}{\sigma}\min_h \phi(h) \tag{51}$$

One easily finds that for $0 \le \theta_S \le \pi/2$, eq 51 results in larger contact angles than eq 50. Note also the steeper fronts in the dewetting profiles for the nonlinear curvature models in ref 26. All these facts may explain the shift in capillary number shown in Figure 7.

Let us for a moment focus on a special region in the $Ca(B)$ plot. There is a specific regime near the transition from oscillatory to monotonic rims where the fitting procedure is not straightforward. Note that the "monotonic" fitting function $\delta\tilde{H}_{mon} = \delta\tilde{H}_1\exp(\Gamma_1\Xi) + \delta\tilde{H}_2\exp(\Gamma_2\Xi)$, which is the solution for real Γ_1 and Γ_2, exhibits a local minimum and approximates zero from negative values if either $\delta\tilde{H}_1$ or $\delta\tilde{H}_2$ is negative. Hence, for profiles showing a local minimum between the rim and the undisturbed film that do not show a clearly pronounced second maximum, both $\delta\tilde{H}_{osc}$ and $\delta\tilde{H}_{mon}$ may capture the data. We have fitted both functions to a number of profiles in that regime and have extracted the slip lengths as well as the respective capillary numbers. The results for B shown in Figure 8 correspond to a growing hole in a 130-nm-thick PS film dewetting from OTS at 110 °C as captured by in situ AFM. For small holes, the function $\delta\tilde{H}_{mon}$ captures the monotonic profiles very well, and the results for the slip length are reasonable. For radii between about 1.5 and 5 μm, the rim profile exhibits a local minimum. The function $\delta\tilde{H}_{mon}$ still captures the rim shapes provided either $\delta\tilde{H}_1$ or $\delta\tilde{H}_2$ is chosen negative; however, the extracted slip lengths

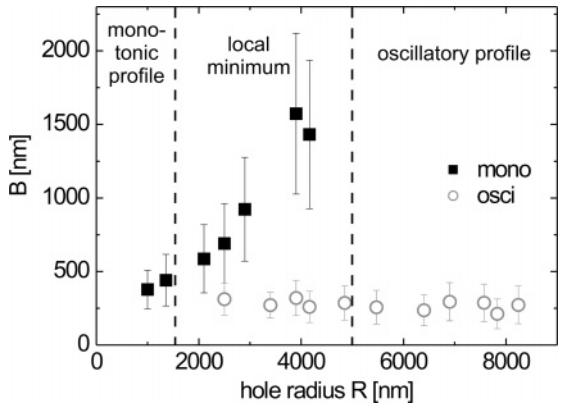

Figure 8. Near the transition between monotonically and oscillatory decaying rims, profiles with a clear minimum can be fitted by both functions $\delta\tilde{H}_{mon}$ and $\delta\tilde{H}_{osc}$. Using the function for real $\Gamma_{1,2}$, $\delta\tilde{H}_{mon}$, the results for B are much larger than for fitting the profiles with $\delta\tilde{H}_{osc}$. The data correspond to a 130-nm-thick PS(13.7k) film dewetting from OTS at 110 °C, as captured by in situ AFM.

are not independent of R. The identical rim profiles fitted by $\delta\tilde{H}_{osc}$ result in a constant slip length. In addition, we found slightly better quality for the fit when using $\delta\tilde{H}_{osc}$ compared to the fit of $\delta\tilde{H}_{mon}$ to the profiles in this regime. For holes with radii larger than 5 μm, the function $\delta\tilde{H}_{mon}$ does not capture the oscillatory rim profiles at all. The described consistency check for various rim sizes provides a general argument that excludes the case of negative coefficients $\delta\tilde{H}_{1,2}$ in the fitting function $\delta\tilde{H}_{mon}$ for real $\Gamma_{1,2}$.

5.3. Limitation of Validity. For the rim analysis described above, we need two inverse decay lengths Γ_1 and Γ_2. However, in the case of extremely large slip lengths and asymmetric rims, the second inverse decay length is too large to be observed experimentally. As a consequence, it is not possible to determine either the capillary number or the slip length solely from the rim profile. However, if the capillary number is measured independently, then one of the inverse decay lengths is sufficient to determine the slip length.[29] In our experiments, the described situation occurs for 130-nm-thick PS(13.7k) films on the DTS coating, dewetting at 105 °C. By using independently measured viscosity and velocity data, the capillary number can be determined. From the fit to the rim profile, we have Γ_1. By inserting Ca and Γ_1 into the characteristic equation (eq 48), the slip length in this situation is found to be about 5 μm, which corresponds to the ratio $b = B/\bar{H} \approx 40$. The same experiment at 110 °C exhibits a slip length of about 3 μm, hence $b \approx 20$. This is approximately the limit up to which both inverse decay lengths Γ_1 and Γ_2 can be extracted from the measured rim profile. For polystyrene films of higher molecular weight (above 100 kg/mol), the rim gets more and more asymmetric,[30] indicating an increasing slip length. Hence, in most cases the slip length is expected to exceed the upper limit of $b \approx 20$.

In the examples described above, we used the strong-slip model to extract the capillary number and the slip length from the rim profiles. However, this model is valid only for slip lengths larger than the film thickness. The smallest B observed in our experiments for PS(13.7) films on OTS at 130 °C was on the order of $\bar{H}$. For systems with much smaller slip lengths, the strong slip model will produce systematic errors. As shown in

(26) Münch, A.; Wagner, B. *Physica D* **2005**, *209*, 178.
(27) Reiter, G.; Khanna, R. *Langmuir* **2000**, *16*, 6351.
(28) Flitton, J. C.; King, J. R. *J. Eng. Math.* **2004**, *50*, 241.

(29) In fact, if the capillary number is known, then one inverse decay length is *always* sufficient to extract the slip length, independent of its value. However, as long as two modes are observable experimentally, it is more accurate to fit both modes.
(30) Seemann, R.; Herminghaus, S.; Jacobs, K. *Phys. Rev. Lett.* **2001**, *87*, 196101.

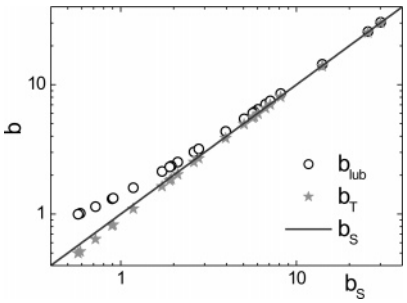

Figure 9. Comparison of slip parameters that yield the same two (real or complex) spatially decaying modes using either the strong-slip model χ_{lub} (open circles), the third Taylor expansion of the Stokes model χ_T (stars), or the full Stokes model χ_S (solid line). The data correspond to the rim profiles analyzed in Figure 6.

Figure 3, the critical dewetting velocity $\dot{s}_{crit}(b)$ as obtained from the strong-slip model significantly deviates from the actual value obtained from the full Stokes model for small b.

The validity and accuracy of the strong slip lubrication approximation can be assessed by comparison with the result for the full Stokes model. Figure 9 shows slip parameters determined by the lubrication model χ_{lub}, $b_{lub} = B_{lub}/\bar{H}$ in comparison to results using the Stokes model χ_S, $b_S = B_S/\bar{H}$. There are quite strong deviations for weak slippage (i.e., for $b < 1$). For rim shape analysis in practice, however, it is not convenient to use the full Stokes model χ_S because the expressions for B_S and Ca_S are rather long and cumbersome, so we use the Taylor approximation that is valid even for weak slippage. The respective characteristic equation (eq 43) in dimensional form is given by

$$\chi_T(\Gamma; B, \mathrm{Ca}) = \left(1 + \frac{\bar{H}}{3B}\right)(\bar{H}\Gamma)^3 + 4\mathrm{Ca}\left(1 + \frac{\bar{H}}{2B}\right)(\bar{H}\Gamma)^2 - \mathrm{Ca}\frac{\bar{H}}{B} = 0 \quad (52)$$

Knowing two roots Γ_1 and Γ_2 of eq 52 from rim shape analysis, we get two equations with the two unknowns B and Ca for which we can solve and obtain

$$B_T = \frac{1}{4\bar{H}}\frac{\Gamma_1^2 + \Gamma_1\Gamma_2 + \Gamma_2^2}{\Gamma_1^2\Gamma_2^2} - \frac{\bar{H}}{2},$$
$$Ca_T = \frac{\bar{H}^3}{6}\frac{\Gamma_1^2\Gamma_2^2}{\Gamma_1 + \Gamma_2} - \frac{\bar{H}}{4}\frac{\Gamma_1^2 + \Gamma_1\Gamma_2 + \Gamma_2^2}{\Gamma_1 + \Gamma_2} \quad (53)$$

Note that the expression for B_T in eq 53 differs from the lubrication result B_{lub} in eq 49 by exactly $\bar{H}/2$. Note also that eqs 52 and 53 are also valid for small values of B (i.e., for the regime in which one would use the weak slip lubrication model that leads to eqs 44). However, using the characteristic equation (eq 44), one cannot determine both Ca and B from the rim shape.

The results for $b_T = B_T/\bar{H}$ are shown in Figure 9 in comparison to the values b_{lub} and b_S. Using the strong-slip lubrication model χ_{lub} instead of the full Stokes model χ_S, the relative error for the extracted slip length increases significantly for decreasing slippage. However, when using χ_T, the deviation of the calculated slip length is quite small, even for weak slippage. Because no limitation for small slip lengths is given for the third-order Taylor expansion of the full Stokes model, the respective equation (eq 53) is recommended for the determination of slippage by rim shape analysis.

6. Conclusions and Outlook

In this article, we have shown both experimentally and theoretically that slippage significantly affects the rim shape of dewetting thin liquid films: slowly moving fronts with no slip or weak slip at the solid/liquid interface develop an oscillatory decaying rim (i.e., complex eigenvalues of the characteristic equation χ of linear stability analysis in a co-moving frame) whereas strong slippage and faster dewetting result in a monotonically decaying shape corresponding to real negative roots of χ. The critical line between complex and real solutions (i.e., where this morphological transition of rim shape occurs) could be very accurately predicted by a new model: instead of using a lubrication model χ_{lub} that accounts only for large slip lengths, we calculated the third-order Taylor expansion χ_T of the characteristic equation obtained from the full Stokes model χ_S. The analytical solution for the transition line using χ_T compares very well to the numerical solution obtained from the Stokes model, even for weak slippage.

Moreover, we developed a method for extracting the slip lengths of dewetting liquid films using rim shape analysis. For short-chain polystyrene films on the DTS coating, we found slip lengths that were about 1 order of magnitude larger than for the same films on OTS. Additionally, on both coatings, the slip length decreases with increasing melt temperature. As already seen for the critical line of the morphology transition, the results for the slip length gained from the lubrication model χ_{lub} are a rather good approximation in the regime of strong slippage. More accurate results for the whole range of slip lengths, however, can be obtained by using χ_T, the third-order Taylor expansion of the full Stokes model.

Acknowledgment. We thank O. Bäumchen for helpful discussions. This work was supported in part by Heisenberg scholarship DFG grant MU 1626/3 (A.M.), the DFG Research Center Matheon Berlin (A.M. and B.W.), DFG grants MU 1626/5 (A.M. and B.W.), RA 1061/2 (M.R.), and Ja 905/3 (K.J.) within the priority program SPP 1164, and the European Graduate School GRK 532 (R.F.). R.F. and K.J. acknowledge the generous support of Si wafers from Siltronic AG, Burghausen, Germany.

LA7010698